

# Calculation of Stark resonance parameters for the hydrogen molecular ion in a static electric field

Ts Tsogbayar and M Horbatsch

Department of Physics and Astronomy, York University, 4700 Keele Street, Toronto, Ontario M3J 1P3, Canada

E-mail: [tsog218@yorku.ca](mailto:tsog218@yorku.ca)

Received 18 January 2013, in final form 5 March 2013

Published 4 April 2013

Online at [stacks.iop.org/JPhysB/46/085004](http://stacks.iop.org/JPhysB/46/085004)

## Abstract

The Schrödinger equation for the  $H_2^+$  ion is solved in prolate spheroidal coordinates using the pseudospectral method. The Stark resonance parameters for the two lowest states of the ion have been determined by adding a complex absorbing potential to the Hamiltonian. The localized electron densities for both (lower and upper) states are obtained to provide explanations for structures seen in the ionization rate as a function of internuclear separation. The Riss–Meyer iterative and Padé extrapolation methods are applied to obtain highly accurate values for the resonance parameters, which are compared to previous results.

(Some figures may appear in colour only in the online journal)

## 1. Introduction

The study of dissociative ionization of diatomic molecules in intense laser fields has been carried out both experimentally [1–9] and theoretically [10–14] following the pioneering theoretical work of [15]. The simplest diatomic molecular ion  $H_2^+$  is a prototype system which can be used to understand intense-field phenomena. For the first excited state (which in the field-free case has ungerade symmetry), the ionization rate as a function of internuclear separation  $R$  shows maxima at some critical separations beyond the equilibrium separation. This enhanced ionization at some larger internuclear separations has been observed experimentally [5, 9] and was discussed on the basis of numerical calculations [10]. In the case of low-frequency ac fields and in the static (dc) field limit, explanations were given for this phenomenon [10–13].

In the presence of an external electric field, the two-centre potential experienced by the electron is distorted: the outer edge of one well is raised, while the outer edge of the other well is lowered, and the reflection symmetry of the electronic potential is destroyed. The lowest gerade and ungerade states of the ion which are nearly degenerate at large  $R$  in the absence of the field are strongly split; the lower state remains in the deeper well, and the other ‘upper’ state is localized in the upper well.

Zuo and Bandrauk [10] observed that the over-the-barrier mechanism is the main reason for the peak in the ionization rate for the upper state as  $R$  is increased. Mulyukov *et al* [12] extended the argument using a somewhat different interpretation for this peak: their argument is based on the curves of the real and imaginary parts of the quasi-energy for varying  $R$ , which is due to the mixing of the upper state with energetically nearby highly excited states that are localized in the lower well. Chu and Chu [13] argued that the charge-resonance effect and multiphoton transitions to the excited electronic states represent the main mechanism responsible for the enhanced ionization phenomenon. In addition, Plummer and McCann [11] reasoned on the basis of localized electron density pictures of the upper resonance state that the critical distances validate a Coulomb explosion model [10, 16], while electron localization and simple over-the-barrier models of electron release are not appropriate mechanisms to explain this phenomenon. Bandrauk and Lu [17] have used time-dependent Schrödinger equation calculations to explore the dc Stark problem of  $H_2^+$  in the presence of an additional magnetic field. Their reported findings and interpretations for the pure Stark problem are also precursors to this work.

In this paper, we report on resonance calculations for the lower and upper states of  $H_2^+$  in the static electric field which are obtained using the complex absorbing potential

(CAP) method for the varying internuclear distance  $R$  to complement previous work [10–14]. To obtain more accurate values of the resonance parameters, the Riss–Meyer iterative method [18] and the Padé approximation and extrapolation to  $\eta = 0$  [19–21] were implemented in analogy to the computationally more restricted work of Mulyukov *et al* [12]. We also show probability densities for both states to support the interpretation of why the ionization rate peaks at particular internuclear separations for two choices of strong-field parameters. This work is restricted to the case where the dc field is aligned with the internuclear axis. This restriction is not considered to be severe, since the  $\text{H}_2^+$  molecule will align prior to ionization [1, 22].

The paper is organized as follows. In section 2, we discuss the fundamental procedures for the determination of both bound and resonance states for the two-centre molecular system with and without the external electric field. In section 3, we present and discuss our results.

## 2. Theory

### 2.1. Bound-state system

The Coulomb two-centre problem for one electron can be solved analytically [23–25]. The field-free electronic Hamiltonian of the  $\text{H}_2^+$  molecule can be written in atomic units as

$$H = -\frac{1}{2}\nabla_{\mathbf{r}}^2 - \frac{1}{|\mathbf{r} + \frac{R}{2}\mathbf{e}_z|} - \frac{1}{|\mathbf{r} - \frac{R}{2}\mathbf{e}_z|}, \quad (1)$$

where  $\mathbf{r}$  is the electron position vector and  $R$  is the internuclear separation.

We transform  $\mathbf{r}$  to prolate spheroidal coordinates  $\mu$ ,  $\nu$  and  $\varphi$ , which are related to the Cartesian coordinates  $x$ ,  $y$  and  $z$  as follows:

$$x = \frac{R}{2}\sqrt{(\mu^2 - 1)(1 - \nu^2)} \cos \varphi, \quad (2)$$

$$y = \frac{R}{2}\sqrt{(\mu^2 - 1)(1 - \nu^2)} \sin \varphi, \quad (3)$$

$$z = \frac{R}{2}\mu\nu, \quad 1 \leq \mu < \infty, \quad -1 \leq \nu \leq 1, \quad 0 \leq \varphi \leq 2\pi. \quad (4)$$

The kinetic energy operator and the Coulomb interaction are written as

$$-\frac{1}{2}\nabla_{\mathbf{r}}^2 = -\frac{1}{2R^2(\mu^2 - \nu^2)} \left( \frac{\partial}{\partial \mu} \left[ (\mu^2 - 1) \frac{\partial}{\partial \mu} \right] + \frac{\partial}{\partial \nu} \left[ (1 - \nu^2) \frac{\partial}{\partial \nu} \right] + \frac{\mu^2 - \nu^2}{(\mu^2 - 1)(1 - \nu^2)} \frac{\partial^2}{\partial \varphi^2} \right), \quad (5)$$

$$V(\mu, \nu) = -\frac{4\mu}{R(\mu^2 - \nu^2)}. \quad (6)$$

The wavefunction can now be expressed in a separable form

$$\Psi(\mu, \nu, \varphi) = \psi_m(\mu, \nu) e^{im\varphi}, \quad (7)$$

and separate eigenvalue problems for different  $|m|$  values are obtained:

$$-\frac{1}{2R^2(\mu^2 - \nu^2)} \left[ \frac{\partial}{\partial \mu} \left[ (\mu^2 - 1) \frac{\partial}{\partial \mu} \right] + \frac{\partial}{\partial \nu} \left[ (1 - \nu^2) \frac{\partial}{\partial \nu} \right] - \frac{m^2}{\mu^2 - 1} - \frac{m^2}{1 - \nu^2} \right] \psi_m - \frac{4\mu}{R(\mu^2 - \nu^2)} \psi_m = E \psi_m. \quad (8)$$

Because the solution for equation (8) is found analytically in terms of Legendre polynomials, it is natural to employ a Legendre-based pseudospectral method. This follows since the zeros of the Legendre polynomials are more densely distributed near  $\nu = \pm 1$  [26, 27]. In this work, we will only consider  $\Sigma$  electronic states ( $|m| = 0$ , no  $\varphi$  dependence); therefore, we will omit the subscript  $m$  from now on.

In the pseudospectral method, we approximate  $\psi(\mu, \nu)$  by  $\psi_{N_\mu, M_\nu}(\mu, \nu)$ :

$$\psi(\mu, \nu) \approx \psi_{N_\mu, M_\nu}(\mu, \nu) = \sum_{i=0}^{N_\mu} \sum_{j=0}^{M_\nu} \phi(\mu_i, \nu_j) g_i[x(\mu)] g_j[y(\nu)]. \quad (9)$$

The independent variables  $\mu$ ,  $\nu$  are transformed into  $x$ ,  $y$ . For our purposes, it is convenient to keep  $\nu = y$ , since  $\nu \in [-1, 1]$ . However,  $\mu$  is mapped according to

$$\mu(x) = 1 + \frac{(1+x)}{2}(b-1), \quad (10)$$

where  $x \in [-1, 1]$  and  $b$  is a mapping range parameter, which defines the size of the elliptic region in which the problem is solved (typically:  $b = 20$  au).

Both cardinal functions  $g_i[x(\mu)]$ ,  $g_j[y(\nu)]$  are defined as [13, 26, 27]

$$g_i(x) = -\frac{1}{N_\mu(N_\mu + 1)P_{N_\mu}(x_i)} \frac{(1-x^2)P'_{N_\mu}(x)}{x-x_i}, \quad (11)$$

$$g_j(y) = -\frac{1}{M_\nu(M_\nu + 1)P_{M_\nu}(y_j)} \frac{(1-y^2)P'_{M_\nu}(y)}{y-y_j}. \quad (12)$$

We have chosen the Legendre Gauss–Lobatto points which take into account both points  $x_0 = y_0 = -1$  and  $x_{N_\mu} = y_{M_\nu} = 1$ , and the internal points are determined by the roots of the first derivatives of the Legendre polynomials  $P_{N_\mu}$  and  $P_{M_\nu}$  with respect to  $x$  and  $y$ , respectively,

$$P'_{N_\mu}(x_i) = 0, \quad P'_{M_\nu}(y_j) = 0. \quad (13)$$

The cardinal functions have the following unique properties which make the matrix calculation easy:

$$g_i(x_{i'}) = \delta_{i,i'}, \quad (14)$$

$$g_j(y_{j'}) = \delta_{j,j'}. \quad (15)$$

After the transformation, the two-dimensional discretized eigenvalue problem (equation (8)) to be satisfied exactly at grid points  $\mu_{i'}$ ,  $\nu_{j'}$  can be implemented directly:

$$\sum_{i'=0}^{N_\mu} \sum_{j'=0}^{M_\nu+1} \left[ -\frac{1}{2} T_{i';i'j'} - \frac{4}{R} \mu_i \delta_{i'i'} \delta_{j'j'} \right] \phi_{i'j'} = E(\mu_i^2 - \nu_j^2) \delta_{i'i'} \delta_{j'j'} \phi_{ij}, \quad (16)$$

$$T_{i';i'j'} = \frac{4}{R^2} [T_{i'i'}^{(\mu)} \delta_{j'j'} + T_{j'j'}^{(\nu)} \delta_{i'i'}]. \quad (17)$$

Here, the partial matrices  $T_{i'i'}^{(\mu)}$ ,  $T_{j'j'}^{(\nu)}$  are related to the coordinates  $\mu$  and  $\nu$ , respectively, and are defined as follows:

$$T_{i'i'} = (\mu_i^2 - 1) \left( \frac{2}{b-1} \right)^2 d_{i'i'}^\mu d_{i'i'}^\mu + 2\mu_i \left( \frac{2}{b-1} \right) d_{i'i'}^\mu, \quad (18)$$

$$T_{j'j'} = (1 - \nu_j^2) d_{j'j'}^\nu d_{j'j'}^\nu - 2\nu_j d_{j'j'}^\nu. \quad (19)$$

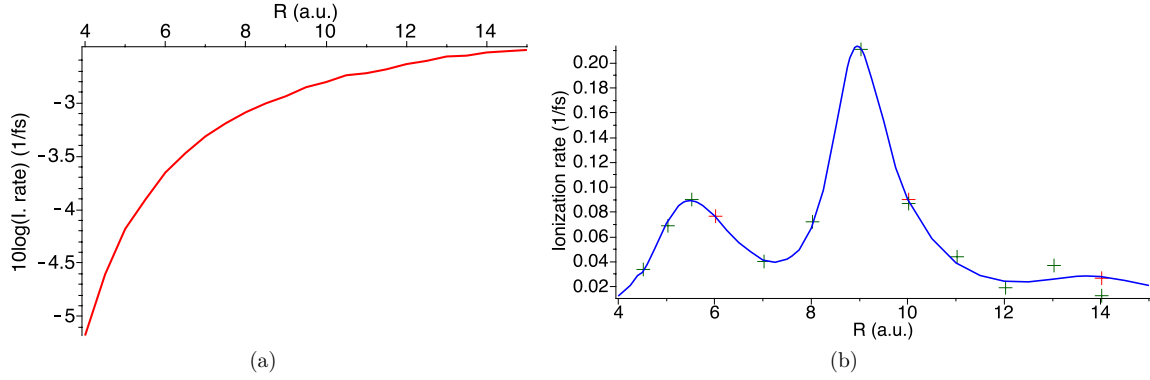


**Figure 1.** The ionization rates (in  $\text{fs}^{-1}$ ) for varying  $R$  for the lower (a), and the upper (b) states for  $\text{H}_2^+$  in  $F = 0.0533$  au. Curves: present results, red crosses: Chu *et al* [13], green crosses: Plummer and McCann [11].

**Table 1.** Some solutions for the  $1\sigma_g$  state of  $\text{H}_2^+$  at  $R = 2.0$  au and  $a = 1, b = 20$ .

$N_\mu$	$M_\nu$	$E_0$	$\langle r^2 \rangle$	$\langle Q \rangle$
12	10	-1.102 363 088 395	2.394 521 797	0.469 280 805
24	10	-1.102 634 214 495	2.394 529 332	0.469 351 782
Exact		-1.102 634 214 495	2.394 529 332	0.469 351 782

The matrices  $d_{ii}^\mu$  and  $d_{jj}^\nu$  are the first-order differentiation matrices using the Legendre Gauss–Lobatto points  $x(\mu_i)$  and  $y(\nu_j)$ , and can be found in a simple closed form [26, 27].

Our approach is very similar to that implemented in [13]. However, instead of using the variational symmetrized method, we employ a direct collocation scheme in equations (16)–(19).

In table 1, we show the eigenenergy of the ground state and expectation values of  $r = (R/2)\sqrt{(\mu^2 + \nu^2 - 1)}$  and  $Q = (3z^2 - r^2)/2$  as a function of the grid parameters  $N_\mu$  and  $M_\nu$  at  $R = 2.0$  au. The collocation method gives excellent results for the moderate values of  $N_\mu$  and  $M_\nu$ .

## 2.2. Stark-resonance Hamiltonian and complex absorbing potential method

The Stark Hamiltonian for the internuclear axis aligned with the field (of strength  $F$ ) written in prolate spheroidal coordinates is given as

$$H_{\text{res}} = -\frac{1}{2}\nabla^2 - \frac{4\mu}{R(\mu^2 - \nu^2)} + F\frac{R}{2}\mu\nu. \quad (20)$$

To avoid the calculation of outgoing waves, we add an artificial complex absorbing potential to this Hamiltonian. One has to choose this complex absorbing potential only for the coordinate  $\mu$ :

$$H = H_{\text{res}} - i\eta W = -\frac{1}{2}\nabla^2 - \frac{4\mu}{R(\mu^2 - \nu^2)} + F\frac{R}{2}\mu\nu - i\eta W, \quad W(\mu) = \Theta(\mu - \mu_c)(\mu - \mu_c)^2, \quad (21)$$

where  $\Theta$  is the Heaviside step function,  $\eta$  is a small positive parameter and  $\mu_c$  determines the ellipse, outside of which the CAP dampens the outgoing wave in the asymptotic region.

This means that the eigenfunction of the resonance state can be solved for in a square-integrable basis, that is, one solves an eigenvalue problem to find complex energy eigenvalues, whose real part yields the resonance position, and the inverse of the imaginary part is associated with the lifetime of that state. While using a finite basis set, ideally we want  $\eta$  to be small to have a small artefact. However, when the parameter  $\eta$  tends to zero, the computational representation error increases. Thus, we want  $\eta$  to be not too small to have an easier or more accurate calculation. Then, we want to remove the artefact due to the CAP. This can be done by the iterative correction method of Riss and Meyer [18], or by a Padé extrapolation method [19–21]. Following [18], we have

$$E^{(n)} = E^{(n)}(\tilde{\eta}) = E_{\text{fb}}(\tilde{\eta}) + \sum_{j=1}^n \frac{(-\tilde{\eta})^j}{j!} \left. \frac{d^j E_{\text{fb}}}{d\tilde{\eta}^j} \right|_{\tilde{\eta}=\tilde{\eta}}, \quad (22)$$

where  $\tilde{\eta}$  is an optimal value found by the condition [18]

$$\left| \frac{\eta^{n+1}}{(n+1)!} \frac{d^{n+1} E_{\text{fb}}}{d\eta^{n+1}} \right|_{\eta=\tilde{\eta}} = \min, \quad n = 0, 1, 2, 3. \quad (23)$$

Here,  $E_{\text{fb}}$  stands for finite-basis eigenvalues calculated on the  $\eta$ -grid.

Following equation (5) in [21], (cf [19]) a Padé approximant for  $E_{\text{fb}}(\tilde{\eta})$  is obtained from

$$E_{\text{Padé}}(\eta) = \frac{\sum_{i=0}^{N_1} p_i \eta^i}{1 + \sum_{j=1}^{N_1+1} q_j \eta^j}, \quad (24)$$

where  $p_i$  and  $q_j$  are complex coefficients, and  $N_p = 2(N_1 + 1)$  is the number of points used in the approximant. We found that  $N_p = 8$  yielded reasonable extrapolations to  $\eta = 0$ .

The discretization procedure for the complex Hamiltonian equation (21) is analogous to the Hermitian case discussed in the preceding subsection.

## 3. Results and discussion

In figure 1, we show the ionization rates for the lower and upper states as a function of internuclear separation  $R$  for the field strength of  $F = 0.0533$  au. The lower state shown in panel (a) displays the monotonic behaviour where the small rate at the natural separation of  $R = 2$  au rises gradually with  $R$  because

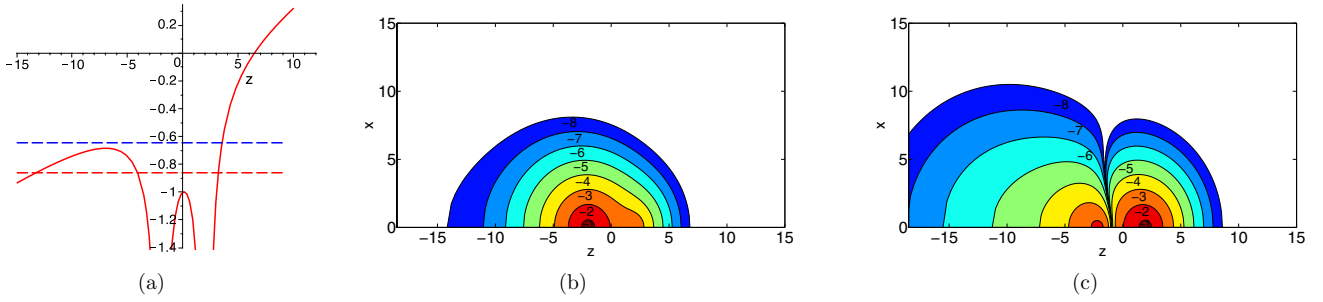


**Figure 2.** Electronic potential and real parts of quasienergies for the lower and upper states (a) and contour plots of  $\log |\psi|^2$  for the lower (b) and upper (c) states for  $\text{H}_2^+$  at  $R = 4$  au and  $F = 0.0533$  au.

**Table 2.** The calculated dc widths  $\Gamma_{\text{low}}$  and  $\Gamma_{\text{up}}$  of the lower and upper states of  $\text{H}_2^+$  in  $F = 0.0533$  au using the stabilization method (SM), Padé extrapolations (PE), and the order ( $n = 3$ ) Riss–Meyer scheme. Also shown are the earlier calculations of Zuo and Bandrauk [10], Mulyukov *et al* [12] and Chu and Chu [13]: the stabilization results (SM) are equivalent to the ( $n = 0$ ) RM results, and the Padé extrapolation is based on complex eigenenergies calculated directly from the non-Hermitian matrix problem for  $\eta$ -values not far from the SM result  $\eta_{\text{SM}}$  ( $\eta > \eta_{\text{SM}}$ ).

	$R = 6$ au		$R = 9$ au	
	$\Gamma_{\text{low}}$ (au)	$\Gamma_{\text{up}}$ (au)	$\Gamma_{\text{low}}$ (au)	$\Gamma_{\text{up}}$ (au)
[10]	2.2(−6)	9.8(−4)		
[12]	5.69(−6)	1.87(−3)		
[13]	5.692(−6)	1.873(−3)		
SM	5.645 17(−6)	1.870 80(−3)	2.958 14(−5)	5.204 57(−3)
PE	5.692 38(−6)	1.873 34(−3)	2.970 75(−5)	5.206 67(−3)
RM ( $n = 3$ )	5.692 38(−6)	1.873 34(−3)	2.970 75(−5)	5.206 67(−3)
	$R = 10$ au		$R = 14$ au	
	$\Gamma_{\text{low}}$ (au)	$\Gamma_{\text{up}}$ (au)	$\Gamma_{\text{low}}$ (au)	$\Gamma_{\text{up}}$ (au)
[10]	1.3(−5)	1.5(−3)	2.5(−5)	2.8(−4)
[12]	3.92(−5)	2.20(−3)	7.30(−5)	6.78(−4)
[13]	3.922(−5)	2.197(−3)	7.305(−5) <sup>a</sup>	6.778(−4)
SM	3.896 99(−5)	2.197 47(−3)	7.304 87(−5)	6.778 81(−4)
PE	3.922 55(−5)	2.196 79(−3)	7.305 23(−5)	6.778 27(−4)
RM ( $n = 3$ )	3.922 55(−5)	2.196 79(−3)	7.305 23(−5)	6.778 27(−4)

<sup>a</sup> Reference [13] shows actually 7.305(−6) which is likely a misprint.

the tunnelling barrier is easier to penetrate, as will be shown in subsequent figures. For the upper state, the much larger ionization rate is non-monotonic and shows strong maxima at  $R \approx 5.5$  au and at  $R \approx 9$  au.

In the latter graph, we show how our results compare with the data of Chu *et al* [13] and Plummer and McCann [11]. Our data are in excellent agreement with those at small and intermediate  $R$ , and confirm the results of [13] at large  $R$ . Our extrapolation and higher order Riss–Meyer results enable us to reach higher accuracy than Chu *et al* and are presented in table 2.

To understand the intriguing behaviour of the upper-state ionization rate, we show plots that indicate the cross section through the potential along the internuclear axis, and also density plots for the resonance states for a few internuclear separations. In figure 2(a), we observe on the basis of the eigenenergies how the lower state is trapped efficiently by the two-centre potential, while the upper state is technically above the potential barrier (shown here just along the internuclear axis). The density plots in parts (b) and (c) of the figure display some preferential localization, as well as a still apparent nodal

structure in the upper state. Nevertheless, both states can still be thought of as exploring the full two-centre potential. In the following, we emphasize the behaviour found for the upper state, since the lower state follows a simple pattern: its tunnelling barrier decreases gradually with separation  $R$  resulting in a monotonic increase in the ionization rate. The upper state, on the other hand, exhibits de-localization and a shift in resonance position as compared to the barrier heights.

In figure 3, we move to the situation where the upper state has a maximum in the ionization rate. The potential barrier between the two protons increases, while the outer potential barrier is lowered. The upper-state energy eigenvalue moves up with increasing  $R$ , which also results in a big increase of the ionization rate. The density plots reveal further localization for the central parts of the resonance wavefunction. The distant parts describe outgoing electron flux. Their relative weight is increased due to the broadening of the resonance state, and the upper state begins to lose its nodal structure.

Figure 4 shows what happens at  $R = 7$  au, where the upper-state ionization rate has a pronounced minimum, but

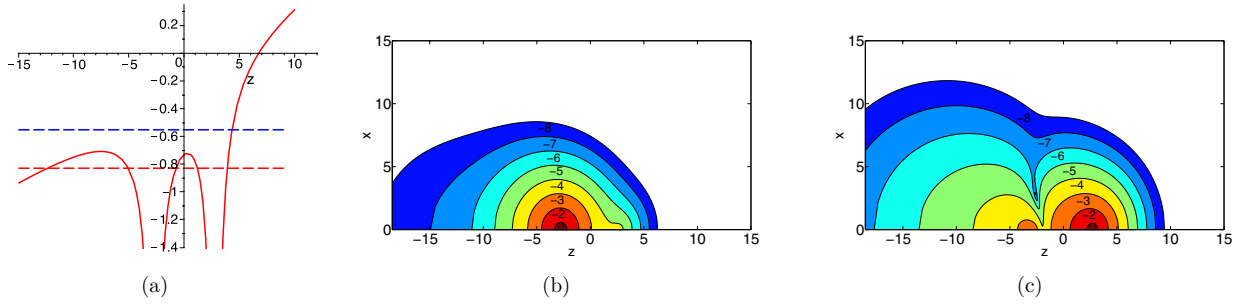


**Figure 3.** The same as in figure 2, but for  $R = 5.5$  au and  $F = 0.0533$  au.

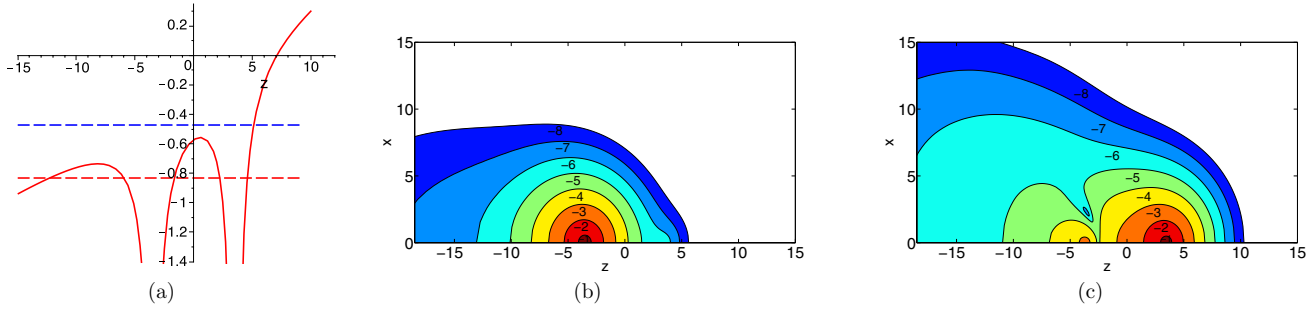


**Figure 4.** The same as in figure 2, but for  $R = 7$  au and  $F = 0.0533$  au.

is still much larger than at  $R = 4$  au. Panel (a) shows that the energetic conditions are less favourable for the upper state than in the  $R = 5.5$  au case, because the inner barrier has risen faster than the energy eigenvalue. The separation of the bound parts of the wavefunctions of the lower and upper resonance states is now very distinct. The outflow of ionized electron density is more de-localized than for smaller separations.

In figure 5, we illustrate the situation for  $R = 9$  au, where the maximum in the upper-state ionization rate is achieved (at more than twice the level of the first maximum). The energy diagram shows that the inner barrier is catching up with the rising upper-state eigenvalue. From the density plot, we can deduce that diffractive scattering is happening from a well-localized bound upper state (note that the lower state is very well confined in the left well), with sideways scattering and forward scattering being the preferred pathways for electron emission.

Further increases in internuclear separation (figure 6 shows the situation for  $R = 14$  au) result in an increased inner barrier height for the upper state. Thus, its ionization rate remains relatively low. The density pattern indicates more diffractive electron emission with less flow in the direction of the internuclear axis.

In order to understand whether these findings are universal, it is useful to consider other field strength values. We have carried out a detailed study of the case of  $F = 0.04$  au. The ionization rates for lower and upper states are shown in figures 7(a) and (b), respectively. The upper-state ionization rate curve again has two maxima with an almost 2:1 ratio for the peak heights. Their positions are shifted to  $R \approx 7.3$  au and  $R \approx 11.2$  au, respectively. As demonstrated in figure 8 for  $R \approx 9.25$  au, the minimum in the ionization rate for the upper state occurs when the eigenvalue is ‘caught’ by the rising potential barrier. Interestingly, for larger separations the barrier

keeps rising, but the system ionizes efficiently by avoiding this region with more sideways electron emission. When going to larger separations ( $R > 13$  au), however, the trapping of the upper state becomes efficient. These findings mostly confirm the conclusions drawn by Plummer and McCann on the basis of complex scaling calculations using an algebraic basis function representation.

We now turn to the problem of a more accurate determination of resonance parameters. While this may be considered a somewhat academic issue, we feel that the hydrogen molecular ion is a fundamental system for which it is useful to have precise benchmark values of complex eigenenergies. In order to reach higher accuracy, one needs to investigate two aspects of the problem. On the one hand, the solution of the discretized problem needs to be analysed with respect to the parameters defining the discretization. We will not report on this convergence study, but claim that we have reached the continuum limit (by careful analysis of how the numbers vary with respect to the basis size). On the other hand, there is the issue that analytic continuation methods introduce the artefact of complex scaling or complex absorption. It is this second issue for which we show some detailed results.

There are two main methods of how to deal with removing such artefacts. The Riss–Meyer method (equations (22) and (23)) is a perturbation-theory-based technique to remove the effects of the complex absorber order by order. Extrapolation of complex eigenvalue trajectories as a function of the CAP strength parameter  $\eta$  is a more direct method, but it requires a careful analysis to ensure that the eigenvalues used in the extrapolation are not contaminated by limitations imposed by the discretization. In principle, by making use of a CAP for which absorption sets in at large distances (analogous to exterior scaling), and where the strength parameter is chosen to be small, one has to represent (outgoing) oscillatory

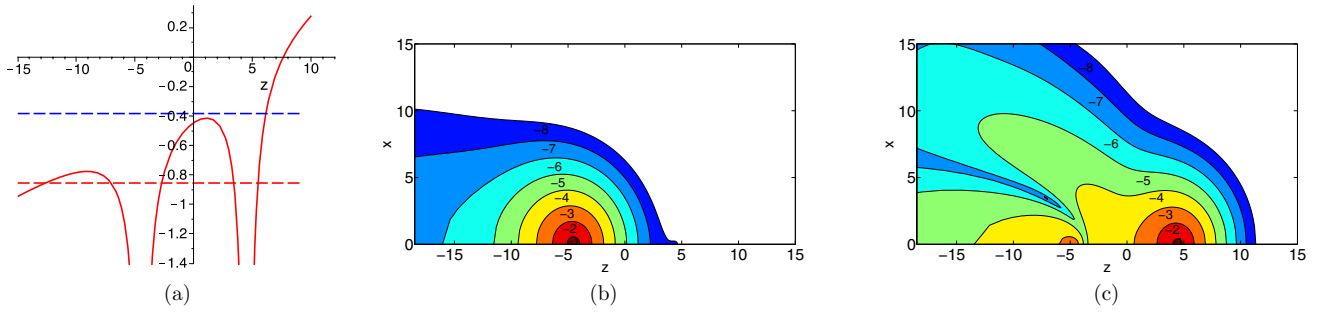


Figure 5. The same as in figure 2, but for  $R = 9$  au and  $F = 0.0533$  au.

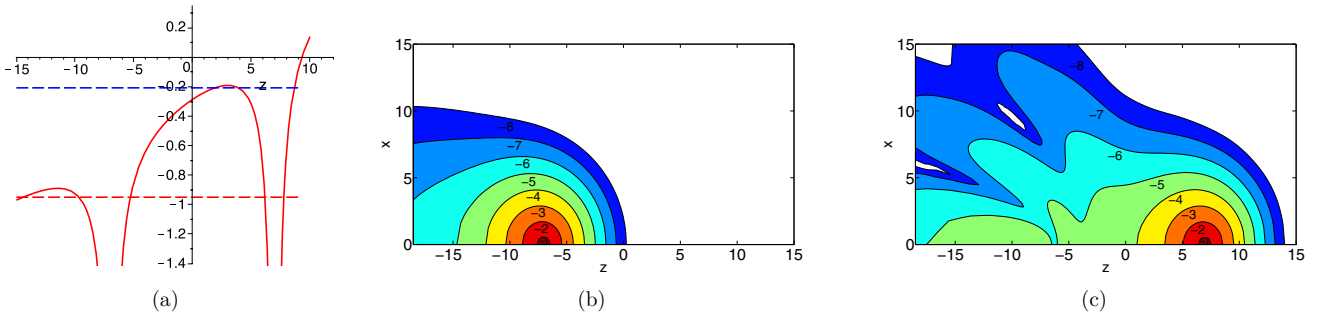


Figure 6. The same as in figure 2, but for  $R = 14$  au and  $F = 0.0533$  au.

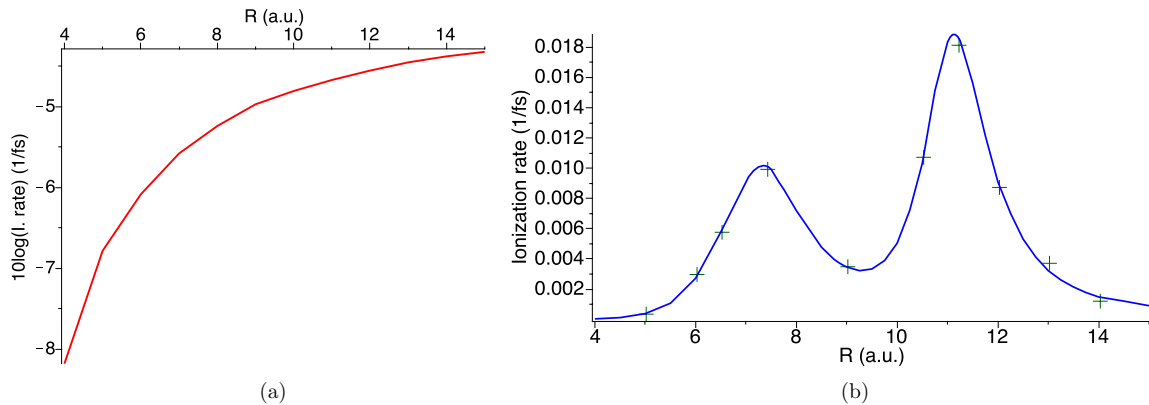


Figure 7. The ionization (in  $\text{fs}^{-1}$ ) rates for varying  $R$  for the lower (a) and the upper (b) states for  $\text{H}_2^+$  in  $F = 0.04$  au. Green crosses: results of Plummer and McCann [11].

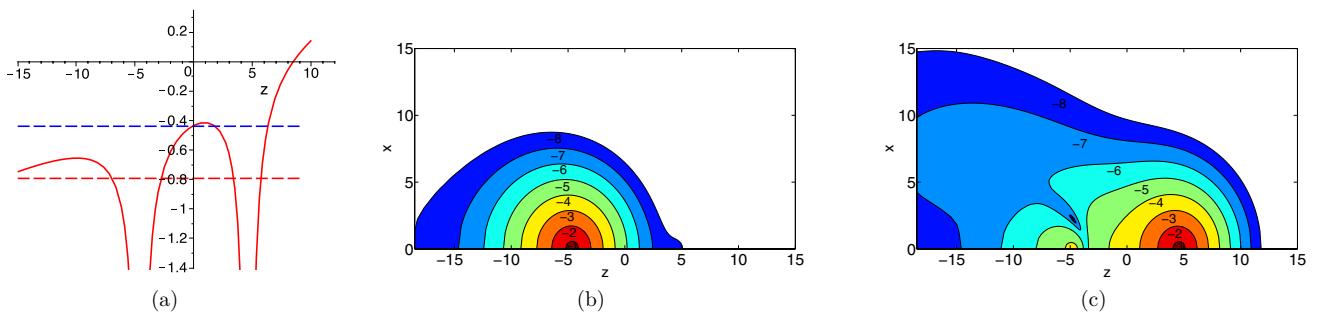
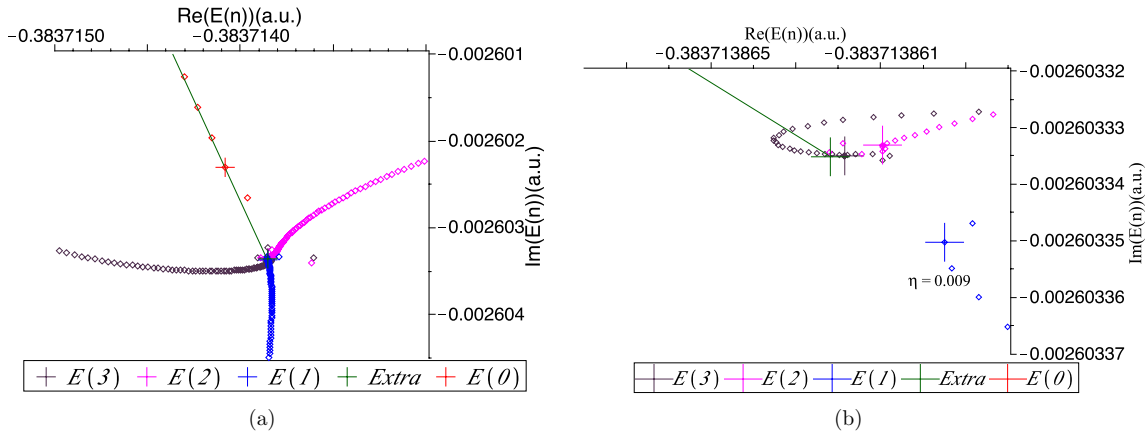


Figure 8. The same as in figure 2, but for  $R = 9.25$  au and  $F = 0.04$  au.

solutions at intermediate distances. If one is not careful, then the discretization method itself prevents the (steady) outflow of density, and one obtains artificial results.

In figure 9(a), we show four basic methods to extract information from the complex eigenvalue trajectories. Shown

as red diamonds are the original finite-basis matrix eigenvalues  $E_{fb}$  near the stabilization value  $\eta_{st}$  (red cross). For  $\eta$ -values less than this stabilization value, the trajectory displays erratic behaviour, since the numerical method cannot handle the demand to compute an outgoing oscillatory solution. When



**Figure 9.** The  $\eta$ -trajectories for  $E^{(0)}$  (red diamonds),  $E^{(1)}$  (blue diamonds),  $E^{(2)}$  (magenta diamonds), and  $E^{(3)}$  (black diamonds) for the upper state of the  $\text{H}_2^+$  ion, and the red, blue, magenta, black and green crosses are for  $E^{(0)}(\tilde{\eta}^{(0)})$ ,  $E^{(1)}(\tilde{\eta}^{(1)})$ ,  $E^{(2)}(\tilde{\eta}^{(2)})$ ,  $E^{(3)}(\tilde{\eta}^{(3)})$ , and the Padé extrapolated values (end point of the green line), respectively. The computational parameters for the upper state at  $R = 9$  au are  $N = 110$ ,  $M = 14$ ,  $\mu_c = 2.2$ . The electric field strength is  $F = 0.00533$  au.

using  $N_p = 8$  accurate eigenvalues from  $\eta > \eta_{\text{st}}$ , a Padé approximation equation (24) is calculated, and this functional form is extrapolated to  $\eta = 0$ . This analytic  $\eta$ -trajectory is shown as a green curve.

Also shown in figure 9(a) are results from the first three orders  $n = 1, \dots, 3$  of the Riss–Meyer iterative correction scheme (equations (22) and (23)). The trajectories  $E^{(n)}(\eta)$  are shown parametrically, and it is evident that on the scale of the graph they have accumulation points equation (23) very close to each other, and that the complex energy values at the accumulation points are very close for  $n = 1, \dots, 3$ , but deviate from the stabilization point ( $n = 0$ ). The proximity to the Padé extrapolation result is also evident.

A magnification of the region close to the  $n = 1, \dots, 3$  accumulation points is shown in figure 9(b). The accumulation points given by equation (23) are marked by crosses and are coinciding with many data points that fall on top of each other. With increasing order  $n$ , the data are based on  $E_{\text{fb}}(\eta)$  values calculated at larger  $\eta$ . For  $n = 1$  (blue symbols), the results at the accumulation point come from the  $\eta = 0.007, \dots, 0.01$  range, for  $n = 2$  (magenta symbols) from  $\eta = 0.009, \dots, 0.024$ , and for  $n = 3$  from  $\eta = 0.013, \dots, 0.042$ . The Padé extrapolated results were based upon  $\eta = 0.007, \dots, 0.014$  and  $\eta_{\text{st}} = 0.003$ . The strength of the higher- $n$  calculations comes, therefore, from the effective removal of the complex-absorber artefacts while using larger values of  $\eta$ . At these larger  $\eta$ -values the solution of the discretized complex Schrödinger problem is closer to the continuum limit, since it involves more localized wavefunctions which are more amenable to a finite representation.

Figure 9(b) allows one to make an assessment of the accuracy level reached by the calculations. Ideally, one would like to demonstrate the convergence of the Riss–Meyer series by showing higher  $n$  results. In practice, these results become affected by differentiation errors along the complex trajectory of  $E_{\text{fb}}(\eta)$ . A conservative estimate of the error would be the difference between the  $n = 2$  and  $n = 3$  results. The Padé extrapolated value falls close to the  $n = 3$  value. Further tests

were performed by varying the value of  $\mu_c$ . Within the range  $1.5 < \mu_c < 3$  (in au), the changes in the accumulation point value for  $n = 3$  remained stable within the tolerance limit mentioned above.

## 4. Conclusions

In this work, we extended previous complex scaling calculations for the Stark resonance problem of the hydrogen molecular ion, which were performed both in algebraic [11, 12] and pseudospectral representations [13] to a higher degree of accuracy by implementing several orders of the Riss–Meyer correction scheme to complex eigenvalues obtained from a pseudospectral calculation with a complex absorbing potential. The surprising behaviour of the ionization rate of the upper state (localized in the higher well) as a function of the internuclear distance was illustrated by density plots of the localized decaying state (whose long-range tails are suppressed by the complex absorber). The computation in prolate spheroidal coordinates is highly efficient. Our previous attempts using cylindrical coordinates were not as successful [29], even though the corresponding Hermitian problem was solved accurately [30].

Some emphasis was placed on the degree of accuracy that can be reached with this method. We intend to apply this methodology to other molecules where the structure problem needs to be addressed with density functional theory. The intent of the work will be to provide other measures than just the ground-state energy and ionization potential for a comparison of different models for the energy functional.

A natural extension of this work would be the ac Stark problem which can be accomplished using a Floquet approach. If one assumes that the strong modulation of the upper-state ionization rate with intermediate separation persists in the case of infrared laser fields, then it follows that the detailed analysis of experiments [31] will be affected by this phenomenon.

## Acknowledgments

We thank the Natural Sciences and Engineering Research Council of Canada for financial support, and the Shared Hierarchical Academic Research Computing Network [32] for access to high-performance computing facilities. We thank Sebastian Ohlmann for contributions during the early stages of the work.

## References

- [1] Codling K and Frasninski L J 1993 *J. Phys. B: At. Mol. Opt. Phys.* **26** 783
- [2] Giust-Suzor A *et al* 1995 *J. Phys. B: At. Mol. Opt. Phys.* **28** 309
- [3] Posthumus J H *et al* 1996 *J. Phys. B: At. Mol. Opt. Phys.* **29** L525
- [4] Constant E, Stapelfeldt H and Corkum P B 1996 *Phys. Rev. Lett.* **76** 4140
- [5] Gibson G N, Li M, Guo C and Neira J 1997 *Phys. Rev. Lett.* **79** 2022
- [6] Stapelfeldt H *et al* 1998 *Phys. Rev. A* **58** 426
- [7] Williams I D *et al* 2000 *J. Phys. B: At. Mol. Opt. Phys.* **33** 2743
- [8] Ergler Th *et al* 2005 *Phys. Rev. Lett.* **95** 093001
- [9] Ben-Itzhak I *et al* 2008 *Phys. Rev. A* **78** 063419
- [10] Zuo T and Bandrauk A D 1995 *Phys. Rev. A* **52** R2511
- [11] Plummer M and McCann J F 1996 *J. Phys. B: At. Mol. Opt. Phys.* **29** 4625
- [12] Mulyukov Z, Pont M and Shakeshaft R 1996 *Phys. Rev. A* **54** 4299
- [13] Chu Xi and Chu S-I 2000 *Phys. Rev. A* **63** 013414
- [14] Peng L-Y *et al* 2004 *J. Chem. Phys.* **120** 10046
- [15] Keldysh L V 1964 *Zh. Eksp. Teor. Fiz.* **47** 1945  
Keldysh L V 1965 *Sov. Phys.—JETP* **20** 1307
- [16] Posthumus J H *et al* 1995 *J. Phys. B: At. Mol. Opt. Phys.* **28** L349
- [17] Bandrauk A D and Lu H Z 2000 *Phys. Rev. A* **62** 053406
- [18] Riss U V and Meyer H-D 1993 *J. Phys. B: At. Mol. Opt. Phys.* **26** 4503
- [19] Lefebvre R, Sindelka M and Moiseyev N 2005 *Phys. Rev. A* **72** 052704
- [20] Santra R 2006 *Phys. Rev. A* **74** 034701
- [21] Ackad E and Horbatsch M 2007 *Phys. Rev. A* **76** 022503
- [22] Bucksbaum P H, Zavriyev A, Muller H G and Schumacher D W 1990 *Phys. Rev. Lett.* **64** 1883
- [23] Hylleraas E A 1931 *Z. Phys.* **71** 739
- [24] Jaffé G 1934 *Z. Phys.* **87** 535
- [25] Baber W G and Hassé H R 1935 *Proc. Camb. Phil. Soc.* **31** 564
- [26] Funaro D 1992 *Polynomial Approximation of Differential Equations* (Berlin: Springer)
- [27] Hesthaven J S, Gottlieb S and Gottlieb D 2007 *Spectral Methods for Time-Dependent Problems* (Cambridge: Cambridge University Press)
- [28] Tsogbayar T 2009 *J. Phys. B: At. Mol. Opt. Phys.* **42** 165007
- [29] Tsogbayar T and Horbatsch M 2013 *Few-Body Syst.* **54** 431
- [30] Fattal E, Baer R and Kosloff R 1996 *Phys. Rev. E* **53** 1217
- [31] Staudte A *et al* 2007 *Phys. Rev. Lett.* **98** 073003
- [32] SHARCNET: Shared Hierarchical Academic Research Computing Network ([www.sharcnet.ca](http://www.sharcnet.ca))